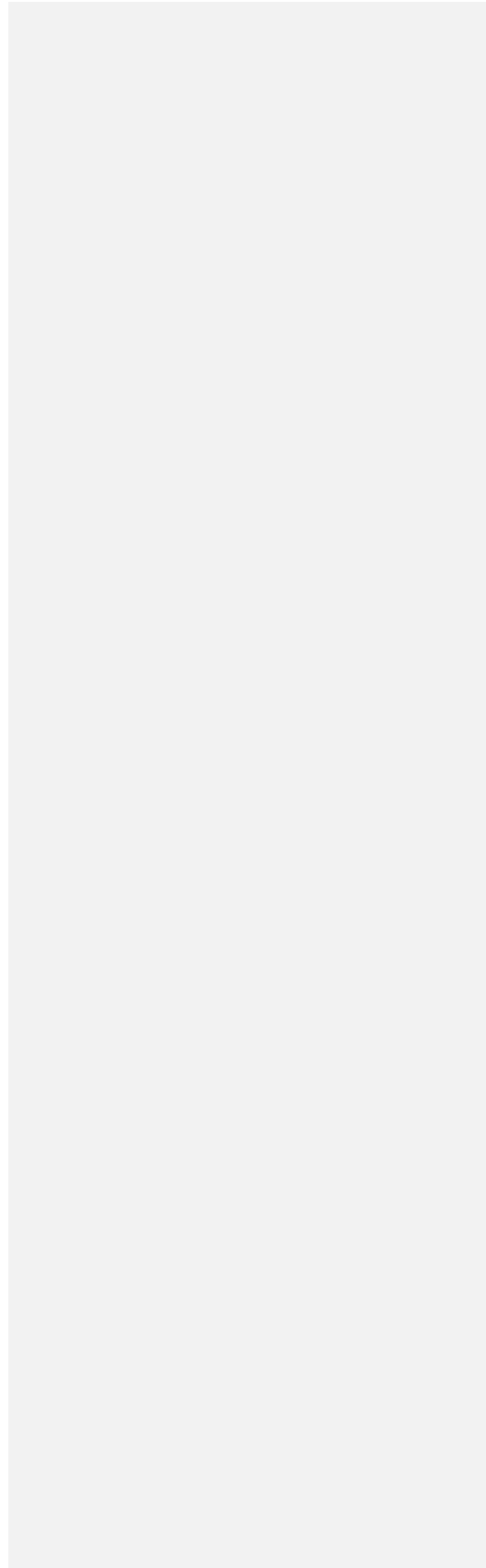


1
2
3
4
5
6
7
8
9
10
11
12
13
14
15
16
17
18
19
20
21
22
23
24
25
26
27
28

**Technical note: determination of the turbulence
demonstrates height of variations in closely
spaced deep-sea mooring lines above
seafloor using turbulence measurements**

by Hans van Haren

Royal Netherlands Institute for Sea Research (NIOZ), P.O. Box 59, 1790 AB Den Burg,
the Netherlands.
e-mail: hans.van.haren@nioz.nl



30 **Abstract.** ~~It may be important to precisely know height variations~~ $O(1)$ m of closely spaced moored
31 oceanographic instrumentation. ~~For example, moorings can be closely spaced or accidentally be located~~
32 ~~on small rocks or in small gullies. Height variations $O(1)$ m will yield registration of different values~~
33 ~~when conditions such as small-scale density stratification vary strongly. Such little height variations~~
34 ~~array prove~~ difficult to measure in the deep sea, requiring high-accuracy pressure sensors preferably
35 on all instruments in a mooring-array. In this paper, an alternative method for relative height
36 determination is presented using 2 -m spaced high-resolution temperature sensors moored on multiple
37 9.5 -m densely-spaced lines in the deep Western Mediterranean. While it was anticipated that height
38 variations between lines could be detected under near-homogeneous conditions via adiabatic lapse rate
39 $O(10^{-4} \text{ } 0.0001^\circ\text{C m}^{-1})$ by the $3 \times 10^{-5} \text{ } 0.00003^\circ\text{C}$ -noise-level sensors, such was prevented by the
40 impossibility of properly correcting for short-term bias due to electronic drift. Instead, a satisfactory
41 height determination was ~~achieve~~ found during a period of relatively strong stratification and large
42 turbulence activity. By band-pass filtering data of the highest-resolved turbulent motions across the
43 strongest temperature gradient, significant height variations were detectable to within ± 0.2 m.

44

45 **1 Introduction**

46 Height variations in moored oceanographic instrumentation can occur above unknown topographic
47 features such as small rocks and gullies and, e.g., due to line stretching under several kN of buoyancy
48 pull. [For example, 0.005-m diameter steel cables \(breaking strength ~20 kN\) stretch about 0.1% of cable](#)
49 [length under 1.25 kN tension, and 0.3% under 4 kN tension for common oceanographic \(e.g.,](#)
50 <https://www.spaceagecontrol.com/calcastre.htm>). If closely-spaced mooring lines and attached
51 instrumentation are used, one may need to correct for the unknown height variations, [for example to be](#)
52 [able to distinguish thin O\(1\) m stratified layers](#). Such a correction is possible using high-resolution
53 temperature sensors.

54 In this technical-performance paper, deep-sea instrumental-height determinations will be
55 demonstrated using 45 mooring lines of 125-m tall and 9.5-m apart horizontally each holding 65 self-
56 contained high-resolution temperature ‘T-’sensors in a 70-m diameter steel-pipe ring (van Haren et al.,
57 2021). Each line, [nylon-coated 0.005-m diameter steel cable](#), was pulled up by a net buoyancy of 1.25
58 kN, imposed by a single buoy on top, and was attached to the anchoring ring via a suspended steel-cable
59 grid. [The problem of this set-up was not so much the vertical-line stretch, but the unknown suspension](#)
60 [of the steel-cable grid. In contrast with a fixed-anchor on a single-line mooring, the steel-cable grid has](#)
61 [different heights between the anchoring steel pipes](#).

62 The ring was moored on a flat seafloor in nearly 2500-m deep weakly density-stratified waters of the
63 Western Mediterranean Sea. The ‘large-ring mooring’ was constructed for three-dimensional studies of
64 deep-sea internal waves, their breaking and turbulence generation, to learn more about their dynamical
65 development via short movies (van Haren et al., 2026) and detailed statistics.

66
67 **2 Materials and Methods**

68 A nearly half-cubic-hectometer of seawater was sampled using 2925 self-contained updated high-
69 resolution, stand-alone T-sensors, new version ‘NIOZ4n’. The ensemble large-ring mooring (Fig. 1a)
70 was deployed in drag-parachute controlled free-fall at the <1° flat and 2458-m deep seafloor of 42°
71 49.50’N, 006° 11.78’E of the Northwestern Mediterranean Sea in October 2020 (Fig. 1b). The mooring
72 was near the site of neutrino telescope KM3NeT/ORCA (Adrián-Martinez et al., 2016) off the coast of

Field Code Changed
Formatted: No underline, Font color: Auto

73 Toulon, France, just 10 km south of the steep continental slope (and 5 km from its foot in the abyssal
74 plain).

75 Fig. 1cb shows the numbering of 45 vertical mooring lines, which were ordered in six groups for
76 synchronisation purposes. As with all NIOZ4 T-sensors (van Haren, 2018), the individual clocks were
77 synchronised via induction to a single standard clock on the mooring-array every 4 hours, so that all T-
78 sensors were sampled within 0.01 s. Three buoys also held a Nortek AquaDopp single-point acoustic
79 current meter. Details of design, construction and deployment are given in van Haren et al. (2021).

80 With the help from Irish Marine Institute Remotely Operated underwater Vehicle (ROV) “Holland
81 I” on board Dutch R/V Pelagia, all lines with T-sensors were successfully cut and recovered in March
82 2024. Of the 45 lines, 43 were in good mechanical order, line 1.8 (line 8 of synchronization group 1;
83 henceforth indicated without decimal point) was hit by the drag parachute whereby 10 sensors were lost,
84 and line 65 was about 0.5 m lower than nominal because of a loop in the vertical line near the cable grid.
85 Only line 36 did not register synchronisation, possibly due to an electric wire failure. Three T-sensors
86 leaked and <10 were shifted in position due to tape malfunctioning. In total 2902 out of 2925 T-sensors
87 functioned as expected mechanically.

88 Due to unknown causes all T-sensors switched off unintentionally when their file-size on the 8-GB
89 Kingston memory card reached 30 MB. It implied that a maximum of 20 months of data was obtained,
90 which were recorded at an interval of once per 2 s. After post-processing, 50-150, depending on moment
91 in the record and type of analysis, extra T-sensors are not further considered due to electronics, noise
92 problems. With respect to previous NIOZ4 version, here named ‘NIOZ4o’, the slightly modified
93 electronics resulted in about twice lower noise levels of 0.00003°C and twice longer battery life.

94 ~~As detailed elsewhere (van Haren, 2018),~~ laboratory-bath calibration yielded a relative precision of
95 <0.001°C (van Haren, 2018). Instrumental electronic drift of typically 0.001°C mo⁻¹ after aging was
96 primarily corrected by referencing daily-averaged vertical profiles, which must be stable from turbulent-
97 overturning perspective in a stratified environment, to a smooth, commonly third-order, polynomial
98 without instabilities (van Haren and Gostiaux, 2012). ~~In addition, b~~Because vertical gradients of
99 temperature, ~~and thus (density) gradients~~ are so small in the deep Mediterranean, so that buoyancy
100 frequency $N = O(f)$, where f denotes the inertial frequency, a secondary drift correction was applied. For

101 [this correction](#), reference was made to periods of typically one-hour duration that were quasi-
102 homogeneous with temperature variations smaller than instrumental noise level (van Haren, 2022). Such
103 >125-m tall quasi-homogeneous periods existed on days 350, ~~(in 2020)~~, 453, and 657, ~~(both)~~ -366 in
104 2021) in the records. ~~These two~~ ~~secondary~~ drift corrections allowed for proper calculations of
105 turbulence values using the method of Thorpe (1977), [as extensively described for moored T-sensors in](#)
106 [van Haren and Gostiaux \(2012\) and van Haren \(2018\)](#), under weakly stratified conditions. As will be
107 demonstrated in Appendix A, under very weakly stratified conditions [with \$N < 0.5\$](#) a tertiary [drift](#)
108 correction involved low-pass filtering of data. This additional correction addresses short-term drift that
109 was about 2-3 times larger in NIOZn than in NIOZo T-sensors.

110

111 3 Results

112 While a single-line mooring attached to an anchor at the seafloor may modify the nominal positions of
113 instrumentation due to buoyancy-stretch of typically 0.1-1% of the total line length, depending on
114 amount of buoyancy and line fabric and make, the large-ring mooring will experience an additional
115 differential positioning due to the variable anchor height of the cable grid. Given the anchor being the
116 steel ring, the distributed buoys on top of each of the 45 lines [are expected to](#) ~~will~~ pull the steel-cable
117 grid (Fig. 1) up in the form of a dome. Hence, different heights are expected for different lines above
118 the, presumed flat, seafloor. [Simple geometrical models mimicking a dome will be compared with](#)
119 [observations of height variations between the different mooring lines.](#)

120 Prior to deployment, stretch-tests were performed with the grid's steel cable [on a harbour quay](#).
121 Under nominal tension of the planned buoyancy it was found that the exerted tension delivered a
122 [measured](#) cable stretch [to a value](#) ~~so~~ that the typical angle of grid inflection was expected to amount 5°.
123 This angle to the horizontal could not be verified from visual inspection using ROV, although at various
124 images a non-zero angle is discernible, which also seems to vary between different cable sections in the
125 grid (Fig. 2a), [as, e.g., in a dome](#).

126 Eight 'corner-lines' (Fig. [1c](#), [2b](#)) were also displaced to an amount not precisely verifiable from
127 ROV-inspection. These lines were attached differently to the steel-cable grid as they could not be
128 attached directly to their intersection points at the steel ring. Estimating the height of corner-line can be

129 attempted from Fig. 2b. Visually, the right side of the small ring holding a vertical line in its center does
130 not touch seafloor and the small ring rotates around the smallest of three short assist cables of which the
131 centre is elevated to approximately $h = 0.6$ m above seafloor. If angles are measured on the basis of
132 vertical/horizontal ratio 4/4.5, then the small-ring makes an angle of about 40° to the horizontal, so that
133 its center is 0.8 m above the edge of the small-ring. In that case, the corner-line will start at $h = 1.0$ m.

134

135 3.1 Parabola model

136 Taking the 5° -angle due to distributed tension stretch as starting point, some simple models of ~~(half-)~~
137 cable-grid cross-section can be made (Fig. 3). Quasi-parabola and straight-cable models are considered.

138 Considering that grid attachments are made in the center of the large-ring pipes at 0.3 m, the models
139 start from that ~~height above seafloor~~. ~~All grid attachments were made to extra enforced steel rings~~
140 ~~that were bolted around the pipes, to guarantee the pipes remain circular. The steel rings and pipes were~~
141 ~~protected against corrosion with zinc anodes (Fig. 2).~~

142 The simplest, albeit unrealistic, straight-cable model makes a fixed angle of 5° (green model in Fig,
143 3). ~~A slightly better model is a paraboloid, a 3D form of the mathematical parabola, as would be~~
144 ~~approximately found in a weighed cable grid held upside down under gravity.~~ A 5-m discretized
145 parabola model intersecting the straight-cable model halfway will have its top at $h = 2.07$ m above (blue
146 model). The steepest part, exceeding 5° , of the cable in this model has a horizontal distance of 5 m to
147 the large ring, which corresponds with the position of, e.g., line 57 (cf. Fig. 1**cb**). In the model, line 57
148 has its lowest T-sensor at $h = 1.2$ m. If an overall maximum angle of 5° is maintained, the top of that
149 parabola model will be at $h = 1.12$ m, and the first line inside the large ring will have its lowest T-sensor
150 at $h = 0.72$ m (red model).

151 In an attempt to verify these cable-grid models, ~~data from~~ the altimeter, and, in a relative sense, the
152 pressure gauge, of the ROV ~~were used. They~~ gave a value of $h = 0.7 \pm 0.1$ m after ~~the ROV had landed~~
153 ~~on the small-ring of the first line of the grid's centre cable, pushing it to the seafloor from the low side.~~

154 -If the maximum- 5° parabola model is correct, all vertical lines are a maximum of 0.4 m, or ± 0.2 m,
155 apart vertically. This is difficult to correct for in practice.

156 Unfortunately no pressure sensors were available [on the vertical lines](#), the three mounted on current
157 meters being too inaccurate, to quantify height variations between lines. As a result, quantification is
158 sought using the T-sensor data to verify, and possibly improve when necessary, above [geometrical](#)
159 model values.

160

161 3.2 Adiabatic lapse rate height-determination method

162 Considering that the T-sensors have a noise level of 0.00003°C, potential temperature differences of
163 $>5 \times 10^{-5} \text{ } 0.00005 \text{ } ^\circ\text{C}$ are statistically significantly detectable, in theory. Thus, given local deep Western
164 Mediterranean adiabatic lapse rate of $\Gamma = -1.7 \times 10^{-4} \text{ } 0.00017 \text{ } ^\circ\text{C m}^{-1}$ (here for simplicity a pressure of 10^4
165 Pa is transferred to a vertical distance of 1 m), vertical height differences of >0.3 m are potentially
166 detectable using T-sensor data under near-homogeneous conditions in which temperature variations are
167 predominantly due to compressibility effects. Such conditions do occur in the deep Western
168 Mediterranean regularly, see the lower 250 m above seafloor in a shipborne-CTD profile (Fig. 4). Γ
169 dominates the temperature lapse with the vertical in Fig. 4a. In time series from moored T-sensor data,
170 near-homogeneous conditions over 125-m vertical range occur about 60% of the time (Fig. 5a). These
171 conditions lead to very low temperature variance across all frequencies outside instrumental white noise
172 (Appendix A).

173 However, a complicating factor in ‘adiabatic lapse rate height-determination’ method is the
174 electronic drift of T-sensors, which varies in intensity per sensor but typically amounts about 10^{-3}
175 $0.001 \text{ } ^\circ\text{C mo}^{-1}$. While the value is one order of magnitude larger than the adiabatic lapse rate per unit
176 length, in principle T-sensors attached to a particular vertical line can be corrected to within a precision,
177 *i.e.* (relative accuracy) of $10^{-4} \text{ } 0.0001 \text{ } ^\circ\text{C}$ (van Haren, 2018). All depends on a calibration with a precision
178 of $<5 \times 10^{-4} \text{ } 0.0005 \text{ } ^\circ\text{C}$, which is achievable using a thermostatic bath with constant temperature levels to
179 within $\pm 10^{-4} \text{ } 0.0001 \text{ } ^\circ\text{C}$ of their preset values. The standard post-processing correction is by fitting a
180 smooth curve over sufficiently time-averaged vertical temperature profile that must be stable over an
181 inertial period. When the temperature range is not too large, above precision is obtainable with some
182 effort and careful search in the data. In the weakly stratified deep Mediterranean however, this correction

Formatted: Superscript

183 is not achievable between different lines, because the low precision is not transferrable to a low absolute
184 accuracy.

185 As a result, the height determinations from translated temperature differences between lines attached
186 to the steel-cable grid are too large and erratically distributed (Fig. 6). Obviously, there is no consistency
187 between lines in the image of Fig. 6, which shows no signs of expected lower ~~(relative)~~ values at the
188 edges close to the ring and higher values near the center, following parabola models as in Fig. 3.
189 Moreover, the variation in values is nearly an order of magnitude greater than expected from the
190 parabola models in Fig. 3. Clustering per calibration -- approximately 190 T-sensors are used in the
191 thermostatic bath per cycle (van Haren, 2018) -- does not give improvement of consistency in the image
192 (not shown).

193

194 3.3 Turbulence variance height-determination method

195 As the adiabatic pressure effect on temperature is not a suitable measuring method for the expected
196 doming of the steel-cable grid inside the large ring, another method is sought. ~~In contrast with the~~
197 ~~adiabatic lapse rate method, this other method is not working under~~ ~~Unexpectedly, such a method is not~~
198 ~~found during a~~ near-homogeneous ~~conditions~~ ~~period~~. Instead, it ~~works~~ ~~is found~~ when vertical temperature
199 stratification is rather large, with peaks resulting in $N = 6f$, and turbulent temperature variations are large
200 (Figs 5a, 7, 8). The combination of these two conditions, relatively large stratification and large
201 turbulence, seems counter-intuitive, as stratification is generally considered to suppress turbulence.
202 Whilst stratification indeed suppresses the vertical length-scale of turbulence, it may have variable
203 effects on temperature variance.

204 In case of the deep Western Mediterranean, relatively large vertical temperature gradients of a few
205 ~~10^{-3}~~ ~~0.001~~ °C over O(10-100) m occur with the advection of warmer waters (Figs 5a, 7a). The advection
206 is ~~regular~~ ~~possibly~~ slanted towards the vertical, either induced by internal-wave action and/or by ~~(sub-~~
207 ~~)mesoscale~~ ~~and mesoscale~~ eddies, ~~as inferred from quasi-3D movies (van Haren et al., 2026)~~. When
208 mainly governed by planetary vorticity deflection, it represents in part convection-turbulence that
209 appears in a vertically stratified environment at mid-latitudes (Marshall and Schott, 1999). All warming
210 events observed thus far associate with considerable turbulence. In the entire time series (Fig. 5a) no

211 significant cooling events occur. Current speeds (Fig. 5b) seldom exceed 0.1 m s^{-1} and thus do not
212 evidence strong flow events such as associated with deep dense-water formation that might occur in late
213 winter, but is not observed.

214 Due to the relatively low-noise T-sensors, deep Western-Mediterranean waters can be characterized
215 by frequency (ω) spectra in which turbulence manifests itself over a range of at least two orders of
216 magnitude (Fig. 8), approximately across $10 < \omega < 3000$ cpd (cycles per day), under the relatively large
217 turbulence conditions. Outside this band, spectra are dominated by internal waves, for $\omega < 10$ cpd, and
218 roll-off to instrumental white noise, for $\omega > 3000$ cpd. A strong temperature gradient produces high-
219 frequency internal waves, but is also accompanied by turbulent eddies, probably as a result of breaking
220 internal waves. Under near-homogeneous conditions similar temperature spectra are found, except that
221 the variance is two orders of magnitude lower and turbulence drops into instrumental noise at about 500
222 cpd (cf. Fig. A2).

223 Here, we take the high-frequency portion $\Theta'(t, z)$ of the well-resolved turbulence band and, somewhat
224 arbitrarily, band-pass filter between $600 < \omega < 1800$ cpd (frequency range indicated by the black bar in
225 Fig. 8) that is certainly outside internal wave and white noise bands. Although temperature variations in
226 this range are part of inertial subrange of isotropic turbulence (Kolmogorov, 1941) reflecting a continual
227 transfer between large energy-containing turbulence scales and small dissipative scales via shear-
228 induced motions, such are mainly found well away from the seafloor. Within $h = O(10)$ m from the
229 seafloor, motions are partly predominantly of isotropic nature and partly of anisotropic convection-
230 turbulence nature in a buoyancy subrange (Bolgiano, 1959; Obukhov, 1959), which manifests at all
231 heights in the range $10 < \omega < 100$ cpd, albeit the spectral smoothing is coarse. Irrespective of a variation
232 in slope and turbulence behaviour, the main goal here is the practical use of temperature (turbulence)
233 variance outlined below. Future investigations will be directed to improve statistics in part by averaging
234 data from the 45 lines and data from different periods of stratified turbulence.

235 During such a period of slanted warm waters from above, temperature variance may be relatively
236 low within a few meters from closest to the seafloor, but it increases to high levels well above common
237 interior-values in the first $O(10)$ m above seafloor (Figs 8, 9). The 1.3-day root-mean-square value of

Formatted: Font: Italic

238 the 600-1800 cpd band-pass filtered signals is calculated for every T-sensor. In this example, the peak
239 in turbulence-temperature variance is found around $h = 11$ m. Above and below the peak one can take
240 advantage of two depth-levels of high gradients in turbulence temperature-variance. Common interior-
241 values are reached at about $h > 40$ m = h_{sst} , which could reflect the upper limit of layer of strong stratified
242 turbulence 'sst' (Figs 7-9).

243 After scaling local turbulence temperature variance $\Theta'^2(z)$ with the 45-line average $\langle \cdot \rangle$ value of its
244 vertical gradient $d\langle \Theta'^2 \rangle / dz$ over $dz = 2$ m, the, here constant, distance between T-sensors, a transfer
245 from temperature to height value is established. Hereby it is assumed that over the 1.3-day period the
246 statistics are homogeneous over the mooring array. Heterogeneity is not expected to affect the average
247 value over a period longer than the inertial period. Subsequently, below or above the peak value in Fig.
248 9, a height pattern can be computed relative to values of an arbitrary vertical line, 44 in this case (Fig.
249 10). Here, the pattern is given for height determination by computing across the largest gradient of
250 temperature-variance, between T-sensors at $h = 3.5$ and 5.5 m#2 and #3 from the seafloor. An example
251 of an eight times shorter period is given in Appendix B.

252 The difference between this pattern and that in Fig. 6 is obvious. First, all values are between 0 and
253 2 m in Fig. 10, and a consistent statistical significance is found to within ± 0.2 m. Cross-sections of the
254 cable grid also confirm the doming of the pattern (Fig. 11). While the observed doming is close to the
255 parabola models of Fig. 3, larger height-determination values than in the models are observed in the
256 center, with slightly steeper overall grid cables that still roughly obey the maximum 5° slopes (Fig. 11).
257 The ± 0.2 -m error range is easily verifiable after comparison with the provided bar. Corrections to
258 vertical positioning of T-sensors are therefore feasible and necessary, because the difference between
259 the center and edges of the cable grid is approximately 1.5 m.

260

261 **3.4 Stratified turbulence quantification**

262 The temperature variations of the well-stratified day 485 demonstrating the necessary height
263 determination for the doming of the steel-cable grid show a background value of turbulence dissipation
264 rate $O(10^{-10})$ $m^2 s^{-3}$. Reduced values $O(10^{-11})$ $m^2 s^{-3}$ are basically only found within a few meters from

265 the seafloor, underneath the largest 2-m small-scale stratification with maximum buoyancy-frequency
266 values of $N_{\max} \approx 1.6 \times 10^{-3} \text{ s}^{-1}$ (Fig. 7). This is observable in time-depth plots of temperature, small-scale
267 stratification and non-averaged turbulence dissipation rate ‘values’. The largest overturns, which
268 dominate the vertically averaged values of turbulence dissipation rate, have a scale $O(100)$ m (Fig. 7a.c).
269 Turbulent overturns reach close to the seafloor, but only sporadically touch it, mostly at begin and end
270 of the warm-water depression. Coarsely every two hours, 124-m vertically averaged turbulence
271 dissipation rate peaks in value (Fig. 2d). ~~indicating the largest overturns being about 100 m in height,~~
272 ~~given a waterflow speed of 0.03 m s^{-1} .~~ ~~Turbulent overturns reach close to the seafloor, but only~~
273 ~~sporadically touch it, mostly at begin and end of the warm water depression.~~ The $h = 40$ m of elevated
274 high-frequency temperature variance (Fig. 9) and stratification (Fig. 7b) show non-negligible turbulence
275 dissipation rate values with further elevated values reaching the seafloor before and after the warm-
276 water passage (Fig. 7c).

277 Time-depth mean values from the 1.3-day period are for turbulence dissipation rate [$\langle \epsilon \rangle$] = $6 \pm 3 \times 10^{-10}$
278 $\text{m}^2 \text{s}^{-3}$ and for turbulent diffusivity [$\langle K_z \rangle$] = $1.4 \pm 0.7 \times 10^{-3} \text{ m}^2 \text{s}^{-1}$ under [$\langle N \rangle$] = $2.8 \pm 0.3 \times 10^{-4} \text{ s}^{-1} \approx 3f$.
279 These 1.3-day, 124-m mean turbulence values are about one order of magnitude larger than open-ocean
280 values observed in stratified waters well away from boundaries (Gregg 1989; de Lavergne et al. 2020;
281 Yasuda et al. 2021). The reader is reminded that the experiment was located close to the foot of the
282 continental slope, where the strong Liguro-Provençal current flows, (internal) tides are weak, and total,
283 (sub-)mesoscale plus near-inertial, water-flow speeds never exceed 0.1 m s^{-1} .

284 Although the warm-water event of Fig. 7 is of relatively strong turbulence, it is not exceptional and
285 elevated temperature-stratification and -variance alternate in time with near-homogeneous episodes
286 throughout the 20-month records (Fig. 5a). This will be reported elsewhere in more detail, notably using
287 three-dimensional investigations.

288
289
290

291 4 Conclusions

Formatted: Superscript

292 The expected height variation due to vertical buoyancy pull across a steel-cable grid, which was
293 suspended within a large anchoring steel-pipe ring, was modelled as an inverted parabolic with
294 maximum 5° angle to the horizontal. To verify the height variation of the instrumented vertical mooring
295 lines across the grid, we expected to use an observational period with ~~negligible~~measurably small vertical
296 density, ~~and thus (temperature,)~~ stratification so that the adiabatic lapse rate $\Gamma = dT/dz$ would dominate
297 vertical temperature variations $T(z)$. The T-sensors have a noise level of about 3×10^{-5} ~~0.00003~~°C, while
298 $|\Gamma| \approx 1.7 \times 10^{-4}$ ~~0.00017~~°C m⁻¹ in the deep Western Mediterranean and thus is potentially measurable by
299 sensors nominally 2-m apart vertically. However, the sensor's electronic drift at all scales turned out
300 insufficiently correctable under near-homogeneous conditions.

301 Instead, a mooring-height determination was ~~achieve~~found during a period of relatively large
302 stratification, during a slump down of warm water presumably slanted from above and induced by
303 internal waves. By band-pass filtering the highest resolved turbulence variance, mainly from inertial
304 subrange, across the strongest temperature gradient, the dome of pulled-up grid was significantly
305 detectable, and fine-tuned a parabola model with height variations between the moorings of correctable
306 $(0.5-2.0) \pm 0.2$ m.

307 The impact of investigating turbulence signals from high-resolution moored T-sensors ~~in~~ the deep
308 Mediterranean is several-fold. First, it demonstrates the dynamics of internal-wave breaking governed
309 by either near-inertial or sub-mesoscale motions slumping relatively warm waters to within a few meters
310 above the seafloor. Thereby, an episodic-average turbulence dissipation rate is provided, which is about
311 ten times larger than ambient values above a flat seafloor. The enhanced turbulence affects deep-sea
312 life. Deep-sea turbulence is studied more elaborately in van Haren (2026 submitted).

313 Second, the strong vertical variation in turbulence temperature-variance profiles, across relatively
314 large local vertical temperature gradients, may be useful for height determinations in nearby moorings
315 over flat seafloors also in shallow seas, and, more difficult, above sloping seafloors, whereby a
316 correction may be applied for ~~(unknown)~~ mooring-line stretch under tensioning by buoyancy. Such
317 height determinations may also be necessary when moorings are accidentally placed on small rocks or
318 in small gullies. The resulting determination demonstrated that the parabola model based on in-house

319 line-tensioning was adequate and required only secondary adjustment in the slightly steeper cables of
320 the underwater large-ring mooring, albeit all showed $<5^\circ$ sloping to the horizontal as anticipated from
321 the in-house tests.

322
323 *Data availability.* Only raw data are stored from the T-sensor mooring-array. Analyses proceed via
324 extensive post-processing, including manual checks, which are adapted to ~~each~~ specific analysis task.
325 Because of the complex processing the raw data from the custom-made T-sensors are not made publicly
326 accessible. Current meter and CTD data are available from van Haren (2025): “Large-ring mooring
327 current meter and CTD data”, Mendeley Data, V1, <https://doi.org/10.17632/f8kfwcvtdn.1>.

328
329

330 *Competing interests.* The author has no competing interests.

331
332 *Acknowledgments.* This research was supported in part by NWO, the Netherlands organization for the
333 advancement of science. Captains and crews of R/V Pelagia are thanked for the very pleasant
334 cooperation. The team of ROV Holland I performed an excellent underwater mission to recover the
335 instrumentation of the large ring. NIOZ colleagues notably from the NMF department are especially
336 thanked for their indispensable contributions during the long preparatory and construction phases to
337 make this unique sea-operation successful. I am indebted to colleagues in the KM3NeT Collaboration,
338 who demonstrated unison to get large-scale infrastructural projects funded. M. de Jong and A. Heijboer
339 helped in securing NWO funding.

340

341 **Appendix A Extra drift correction for T-sensors in near-homogeneous waters**

342 When waters are very weakly stratified or near-homogeneous with $N < 0.5\sigma_\theta$ over the range of moored
343 T-sensors, a short-term drift error may emerge. This drift partially causes the impossibility to determine
344 instrumental height variations under such conditions. Albeit electronic drift is well known to occur on
345 long timescales of weeks-months, short-term hourly drift may appear because of nonlinear temperature
346 dependency and/or inadequate contact between the Negative Temperature Coefficient NTC thermistor's
347 and the environment through the glass tube and its contact paste. ~~Negative Temperature Coefficient~~
348 ~~'NTC'~~ thermistors are the measuring component of NIOZ T-sensors. This short-term drift was
349 previously observed in NIOZ4o deep-trench data and, especially clear, in air (van Haren and Bosveld,
350 2022). It turned out difficult to correct for. During a 2017/2018 test experiment in the deep Western
351 Mediterranean it did not pose a great problem in NIOZ4o data. Unfortunately, NIOZ4n appear to have
352 about twice larger short-term drift than previous NIOZ4o, despite their smaller long-term drift and
353 smaller instrumental noise, both by a factor of two-three approximately. A correction for short-term drift
354 of NIOZ4n is proposed below, with reference to NIOZ4o.

355 Half-day NIOZ4n data (Fig. A1a-c) from arbitrary line 25 are compared with a 104-m tall set of
356 NIOZ4o data (Fig. A1d-f). The investigated samples are from almost homogeneous waters, with a total
357 colour-range over a Conservative-Temperature difference of only $1.7 \times 10^{-4} 0.00017^\circ\text{C}$, for both data
358 sets. Although NIOZ4o are more noisy (Fig. A1a,d), the NIOZ4n show a more horizontal-stripy pattern
359 that has different values through time, compared to T-sensors above and below. This is evidence of
360 remaining bias due to short-term drift. Low-pass time filtering, with a cut-off frequency of 500 cpd,
361 does not reduce these (Fig. A1b,e), but additional vertical filtering, with a cut-off wavenumber at 10
362 cpm, adequately removes the bias (Fig. A1c,f).

363 As a consequence of near-homogeneity, energetic overturning scales are expected to be large due to
364 the reduced restoring force. In both data sets in the center of images, albeit clearer in the NIOZ4o, one
365 notices a slanting jet of warmer waters over a vertical range of about 60 m in short bursts of 10-20 m.
366 Such jets of convection turbulence were found abundant in the Mariana Trench (van Haren, 2023), but
367 relatively rarely in the deep Mediterranean.

368 Depending on the rate of stratification, the vertical filter cut-off at 0.05-0.2 cpm (cycles per meter)
369 is obtained after fine-tuning in an attempt to retain the relevant overturning scales as much as possible.
370 Under weakly but stable stratified conditions 0.1-0.2 cpm is used, while under near-homogeneous and
371 unstable conditions 0.05-0.1 cpm is used. The fine-tuning of the vertical filter concerns relatively
372 adequate spectral improvement and turbulence calculations. Naturally, all data-corrections yield a
373 certain loss of information, but it is informative to estimate how much the loss may be.

374 In 4-d-average spectra (Fig. A2) that include the 0.5-d period of Fig. A1, the impact of small-scale
375 drift is seen to be larger for NIOZ4n (Fig. A2a) than for NIOZ4o (Fig. A2b). In these plots spectra are
376 scaled with the slope of buoyancy subrange, for clarity. As a reference for the correction, the temperature
377 difference $\Delta\Theta$ (magenta spectrum) is taken between the two neighbouring T-sensors at $h = 29$ and 31
378 m. That difference spectrum is compared with the spectrum of temperature data from the upper T-sensor
379 (green). The magenta spectrum has a higher noise level by about a factor of two for $\omega > 100$ cpd than
380 that of the green spectrum. This is commensurate with random white noise.

381 At lower frequencies, the magenta spectrum crosses the green spectrum around 50 and 150 cpd for
382 Fig. A2a and A2b, respectively. This means that data are no longer dominated by white noise, but by
383 other parametrizations, which are governed either by natural processes or by instrumental flaws other
384 than noise. Around the crossing frequency, temperature spectra become horizontal following buoyancy-
385 subrange scaling, ~~rather abruptly~~. This scaling, which represents convection turbulence of an active
386 scalar (Bolgiano, 1959; Obukhov, 1959), was no longer dominant at frequencies higher than that of the
387 crossing, more so in Fig. A2**b** than in Fig. A2**a**.

388 After correction by applying vertical low-pass-filtering (red), the weak slope towards lower
389 frequencies, ~~(especially that of Fig. A2a,)~~ is correctly removed and white noise levels are lower. The
390 spectral slope change to white noise is now at the same frequency, 400 cpd, for both data sets. The quasi-
391 transfer function of correction depicted in the blue spectra is less steeply sloping for $\omega < 1000$ cpd in
392 Fig. A2a than in Fig. A2b, which demonstrates the larger effects of short-term drift correction for the
393 NIOZ4n compared to the NIOZ4o. However, in both data sets of very weakly stratified deep-sea waters

394 it prevents resolution of the transition from buoyancy and/or inertial subranges to the viscous turbulence
395 dissipation range.

396 Resuming, after vertical-filtering correction, temperature data at $\omega < 400$ cpd seem useful for
397 turbulence calculations under weakly stratified conditions. Note that this correction is not needed during
398 periods with relatively large temperature variance and stratified, generally more shear-induced,
399 turbulence. For turbulence dissipation rate calculations, 10-30% reduction is obtained from short-term
400 drift correction. This reduction is well within the error range of a factor of two normally achieved for
401 ocean turbulence data.

402

403 **Appendix B Height determination from a short warm-water period**

404 Naturally the method sketched in Section 3.3 does not work under all circumstances. One requires a
405 rather vigorous appearance of stratified warm-water turbulence to preferably reach close to the seafloor.
406 Such periods are sought manually. Even a short 3.6-h period returns a reasonable estimate of the cable
407 grid height (Fig. A3). It mimics Fig. 10, and has some larger noise level with values that remain within
408 the error bar.

409

Formatted: Indent: First line: 0"

410 **References**

- 411 [Adrián-Martínez, S., Ageron, M., Aharonian, F., Aiello, S., Albert, A., Adrián-Martínez, S.](#) et al.: Letter
412 of intent for KM3NeT 2.0, *J. Phys. G*, 43, 084001, 2016. [DOI 10.1088/0954-3899/43/8/084001](https://doi.org/10.1088/0954-3899/43/8/084001)
- 413 Bolgiano, R.: Turbulent spectra in a stably stratified atmosphere, *J. Geophys. Res.* 64, 2226-2229, 1959.
414 <https://doi.org/10.1029/JZ064i012p02226>
- 415 de Lavergne, C., Vic, C., Madec, G., Roquet, F., Waterhouse, A. F., and Whalen, C. B. et al.: A
416 parameterization of local and remote tidal mixing, *J. Adv. Mod. Earth Sys.*, 12,
417 e2020MS002065, 2020. <https://doi.org/10.1029/2020MS002065>
- 418 Gregg, M. C.: Scaling turbulent dissipation in the thermocline, *J. Geophys. Res.*, 94, 9686-9698, 1989.
419 <https://doi.org/10.1029/JC094iC07p09686>
- 420 IOC, SCOR, and IAPSO: The International Thermodynamic Equation of Seawater – 2010: Calculation
421 and Use of Thermodynamic Properties, Intergovernmental Oceanographic Commission,
422 Manuals and Guides No. 56, UNESCO, Paris (F), 196 pp, 2010.
423 <https://unesdoc.unesco.org/ark:/48223/pf0000188170>
- 424 [Kolmogorov, A. N.: The local structure of turbulence in incompressible viscous fluid for very large](#)
425 [Reynolds numbers, Dokl. Akad. Nauk SSSR, 30, 301-305, 1941.](#)
- 426 Marshall, J., and Schott, F.: Open-ocean convection: Observations, theory, and models, *Rev. Geophys.*,
427 37, 1-64, 1999. <https://doi.org/10.1029/98RG02739>
- 428 Obukhov, A. M.: Effect of buoyancy forces on the structure of temperature field in a turbulent flow,
429 *Dokl. Akad. Nauk SSSR*, 125, 1246-1248, 1959.
- 430 Thorpe, S. A.: Turbulence and mixing in a Scottish loch, *Phil. Trans. Roy. Soc. Lond. A*, 286, 125-181,
431 1977. <https://doi.org/10.1098/rsta.1977.0112>
- 432 van Haren, H.: Philosophy and application of high-resolution temperature sensors for stratified waters,
433 *Sensors*, 18, 3184, doi:10.3390/s18103184, 2018. <https://doi.org/10.3390/s18103184>
- 434 van Haren, H.: Thermistor string corrections in data from very weakly stratified deep-ocean waters,
435 *Deep-Sea Res. I*, 189, 103870, 2022. <https://doi.org/10.1016/j.dsr.2022.103870>
- 436 van Haren, H.: How and what turbulent are deep Mariana Trench waters? *Dyn. Atmos. Oc.*, 103, 101372,
437 2023. <https://doi.org/10.1016/j.dynatmoce.2023.101372>

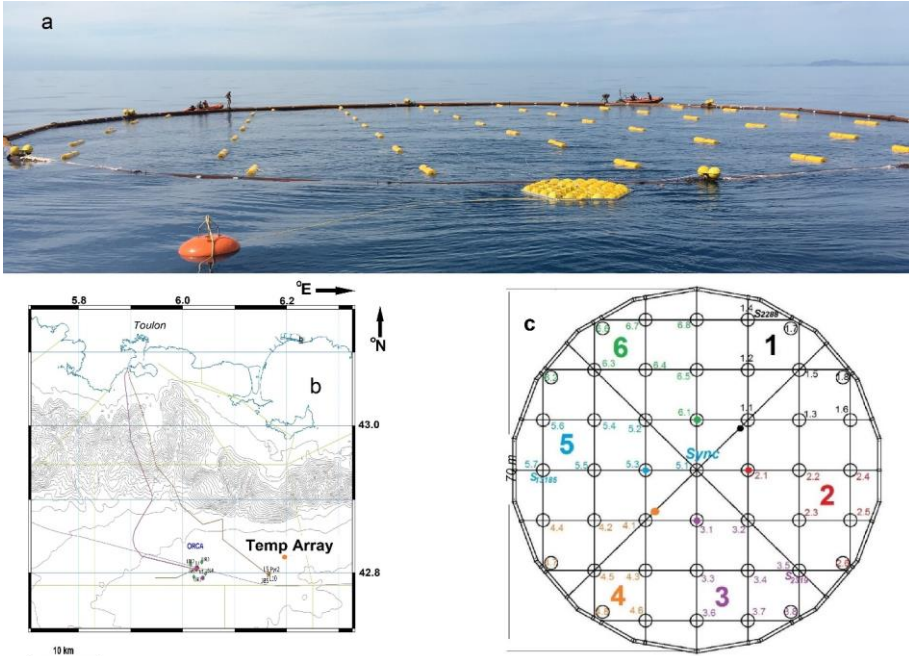
438 van Haren, H., and Bosveld, F. C.: Internal wave and turbulence observations with very high-resolution
439 temperature sensors along the Cabauw mast, *J. Atmos. Ocean. Technol.*, 39, 1149-1165, 2022.
440 <https://doi.org/10.1175/JTECH-D-21-0153.1>

441 [van Haren, H. and Gostiaux, L.: Detailed internal wave mixing observed above a deep-ocean slope, *J.*](#)
442 [Mar. Res.](#), 70, 173-197, 2012.
443 https://elischolar.library.yale.edu/journal_of_marine_research/337

444 van Haren, H., Bakker, R., Witte, Y., Laan, M., and van Heerwaarden, J.: Half a cubic hectometer
445 mooring-array 3D-T of 3000 temperature sensors in the deep sea, *J. Atmos. Ocean. Technol.*,
446 38, 1585-1597, 2021. <https://doi.org/10.1175/JTECH-D-21-0045.1>

447 van Haren, H., [Adriani, O.](#), [Albert, A.](#), [Alhebsi, A. R.](#), [Alshalloudi, S.](#), et al.: Whipped and mixed warm
448 clouds in the deep sea, *Geophys. Res. Lett.*, [53](#), [e2025GL119998](#)~~in press~~, 2026.
449 <https://doi.org/10.1029/2025GL119998>

450 Yasuda, I., [Fujio, S.](#), [Yanagimoto, D.](#), [Lee, K.J.](#), [Sasaki, Y.](#), et al.: Estimate of turbulent energy
451 dissipation rate using free-fall and CTD-attached fast-response thermistors in weak ocean
452 turbulence, *J. Oceanogr.*, 77, 17-28, 2021. <https://doi.org/10.1007/s10872-020-00574-2>
453



454



455

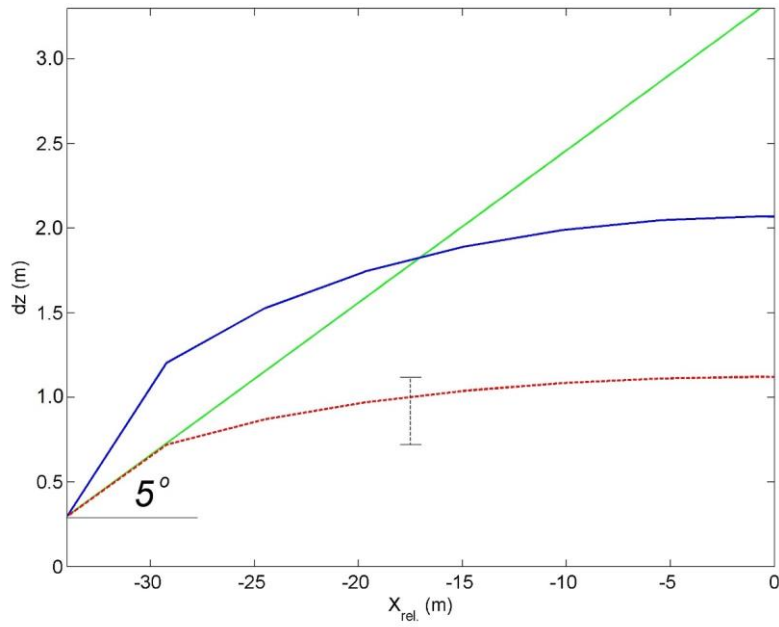
456 **Figure 1.** Large ring in fold-up form at sea, during deployment just prior to finish the opening of air-
 457 valves. The front part of the large steel-pipe ring is already underwater. Almost all top-buoys of the 45
 458 small-ring-compacted mooring lines are visible. In the front still outside the ring, the yellow drag
 459 parachute and orange pick-up buoy are floating. (b) Location named "Temp Array" (orange dot) off
 460 southern France. The mooring is well east of main neutrino telescope 'NT' site "ORCA" of KM3NeT
 461 (Adrián-Martinez et al., 2016) and just northeast of the former ANTARES NT-site. Isobaths are given
 462 every 100 m. (c) Layout of the large-ring mooring viewed from above, with steel-cable grid and small-

463 rings numbered in six synchronisation groups. Lines 14, 35 and 57 (omitting the decimal point) held a
464 current meter at the top-buoy. Corner-lies are, in clockwise direction: 17, 18, 26, 38, 48, 47, 62 and 66.
465

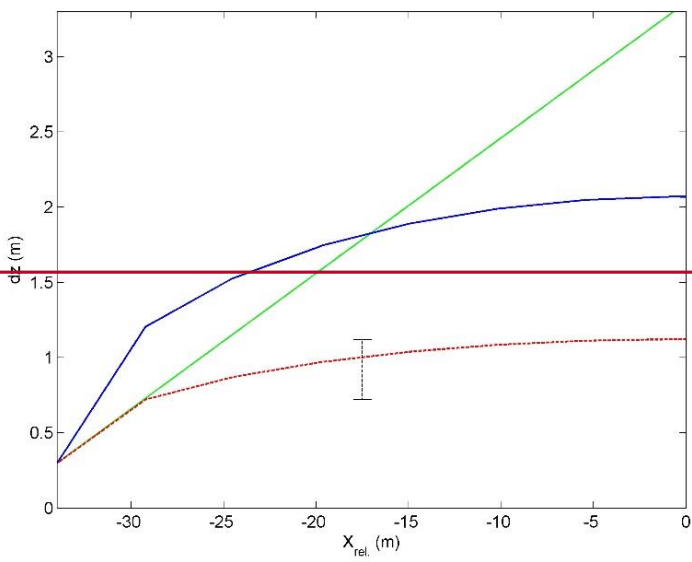


466
 467 **Figure 2.** Underwater video stills of small-rings demonstrating steel-cable grid elevation and cable-
 468 inclinations. The 0.61-m diameter steel pipe in the foreground is part of the large anchoring ring, which
 469 sank 0.07 ± 0.02 m in the sediment of the $< 1^\circ$ flat seafloor. All steel cables are attached to the middle of
 470 the steel pipes, and thus at height $h = 0.24$ m above sediment. (a) Line 44 (cf. Fig. 1**cb**). To the right of
 471 the small-ring the wire visibly makes a larger angle to the ~~horizontal~~vertical than to the left. (b) Estimating
 472 height of ‘corner-line’ 47, see text. (Images from video by ROV Holland I).

473



474

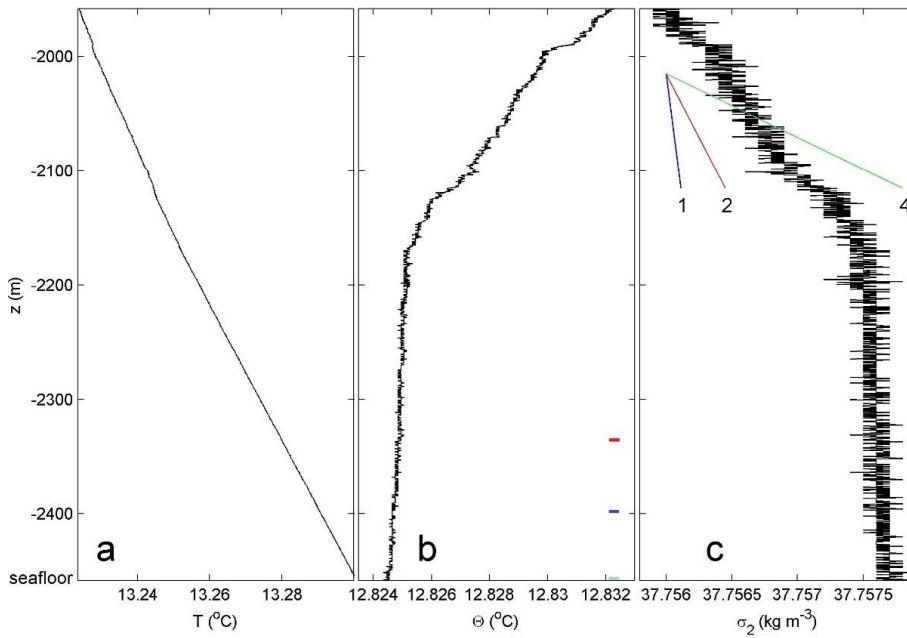


475

476 **Figure 3.** Some expected quasi-parabola and straight-line models, for half centre steel cable of large-
 477 ring mooring grid. The seafloor is at the horizontal axis, the cable-grid attachment to the large-ring is
 478 for a steel pipe at a solid floor. The green straight line makes a fixed angle of 5° with the horizontal,
 479 which angle was established after in-port tension tests. The blue (solid line, 5-m discretized) parabola
 480 model intersects the green line halfway, so that its top is at $h = 2.07$ m. If an overall maximum angle of
 481 5° is maintained (red dashed model), the parabola top is at $h = 1.12$ m, and the first vertical line
 482 attached to relative horizontal position $x_{rel} = -29$ m will be at $h = 0.72$ m.

Formatted: Font: Not Bold

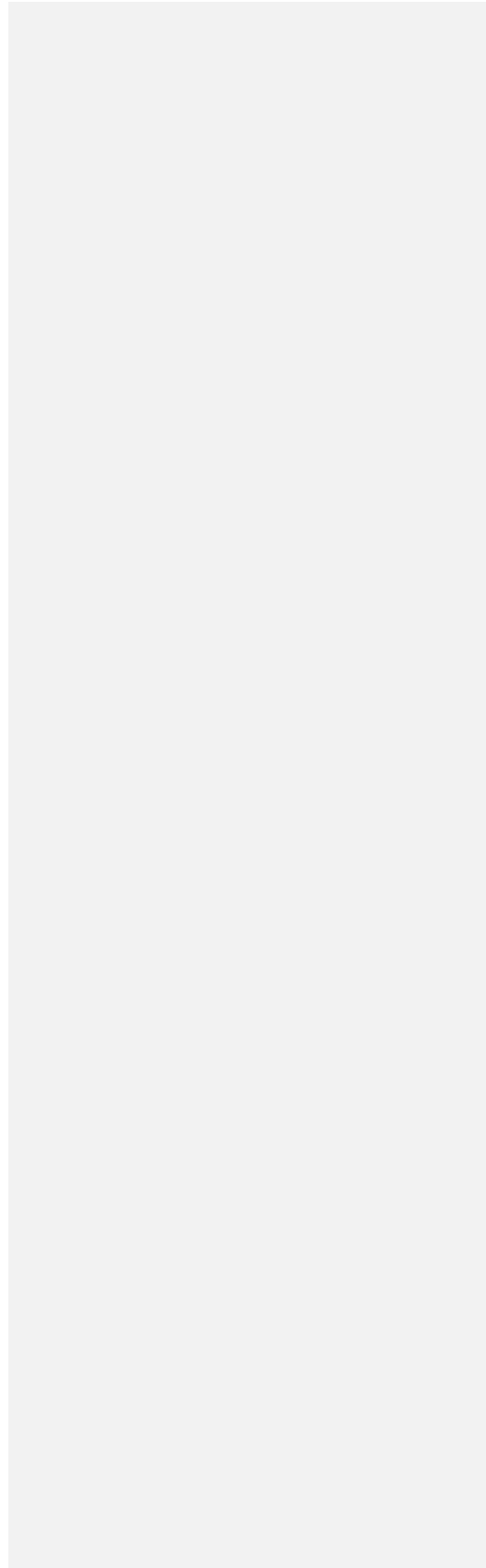
483

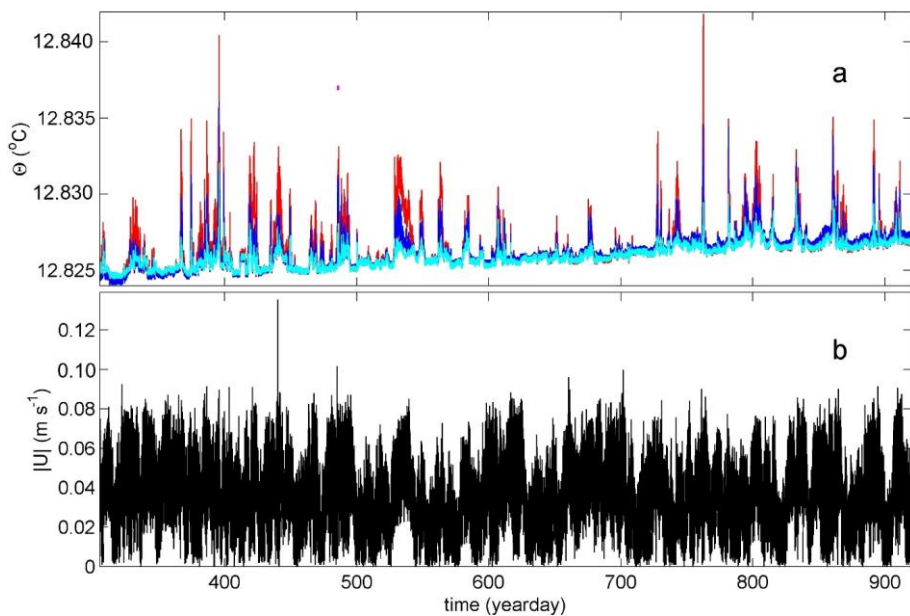


484

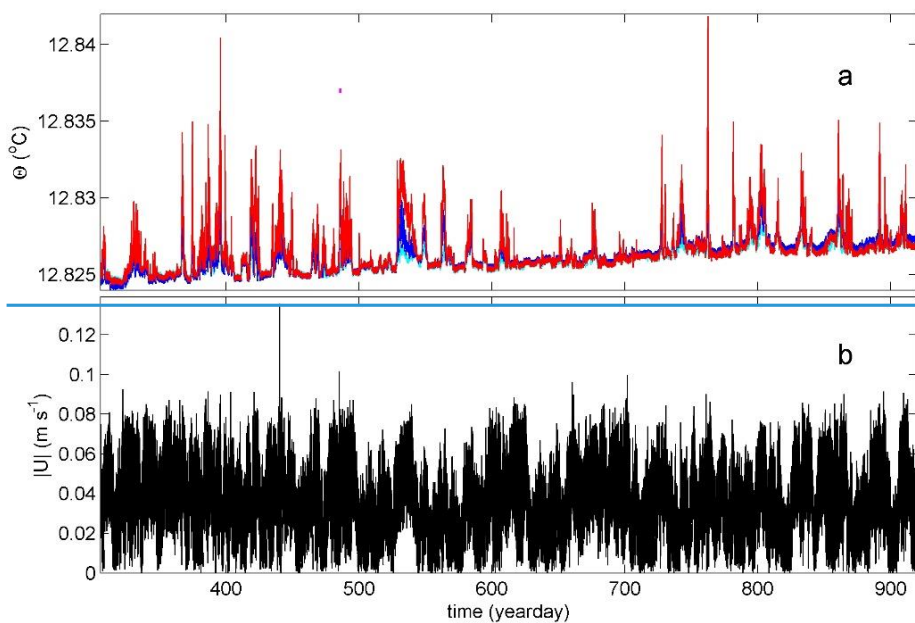
485 **Figure 4.** Lower 500 m of shipborne CTD-profile data obtained near the large ring during mooring
 486 deployment. (a) In situ uncorrected temperature. (b) Conservative Temperature (IOC et al., 2010), data
 487 in a. corrected for compression. Small colour bars indicate nominal heights of moored T-sensors at
 488 lowest (cyan), middle (blue) and upper (red) positions. (c) Density anomaly referenced to 2×10^7 Pa. The
 489 sloping lines indicate several stratification rates in terms of buoyancy frequency $N = xf$, $x = 1, 2, 4$ times
 490 the local inertial frequency f .

491



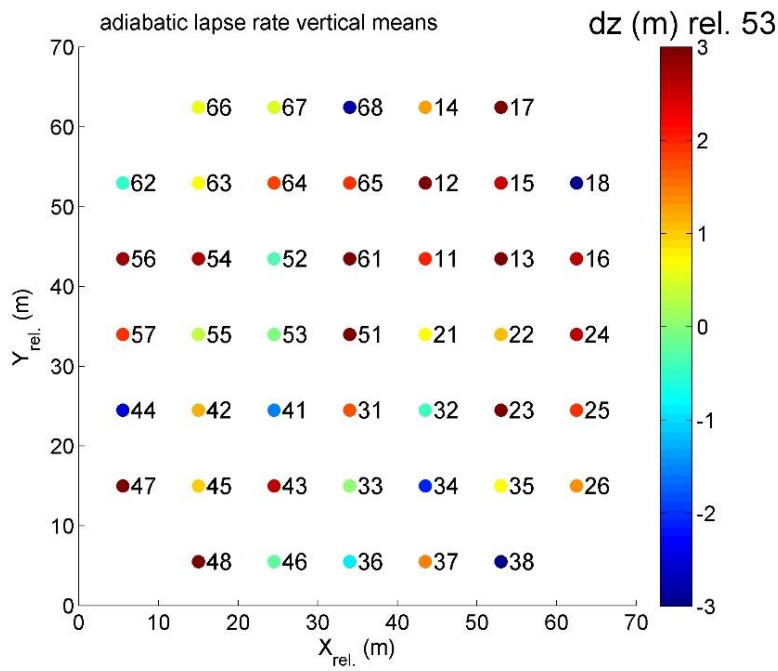


493

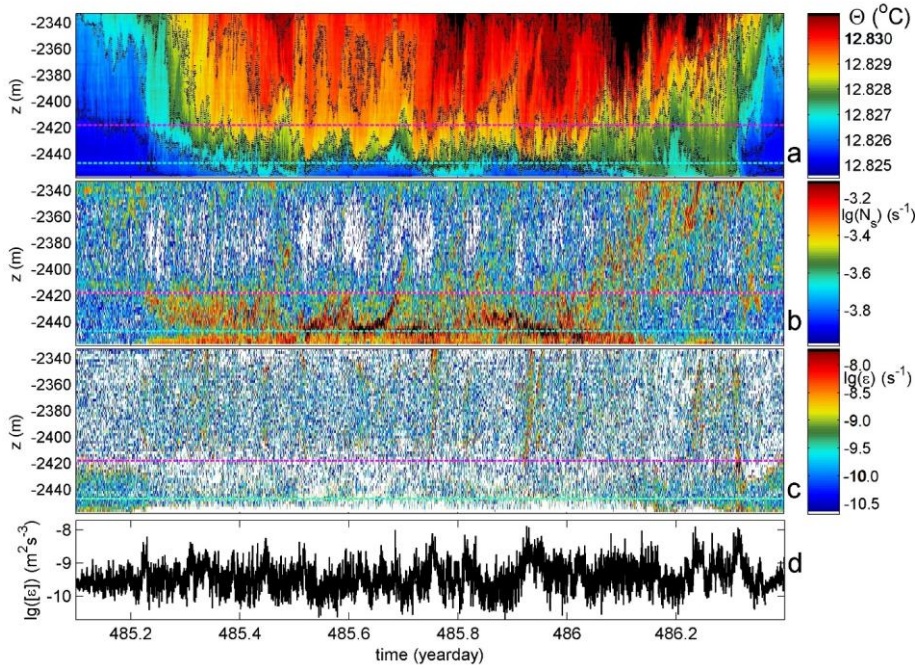


494

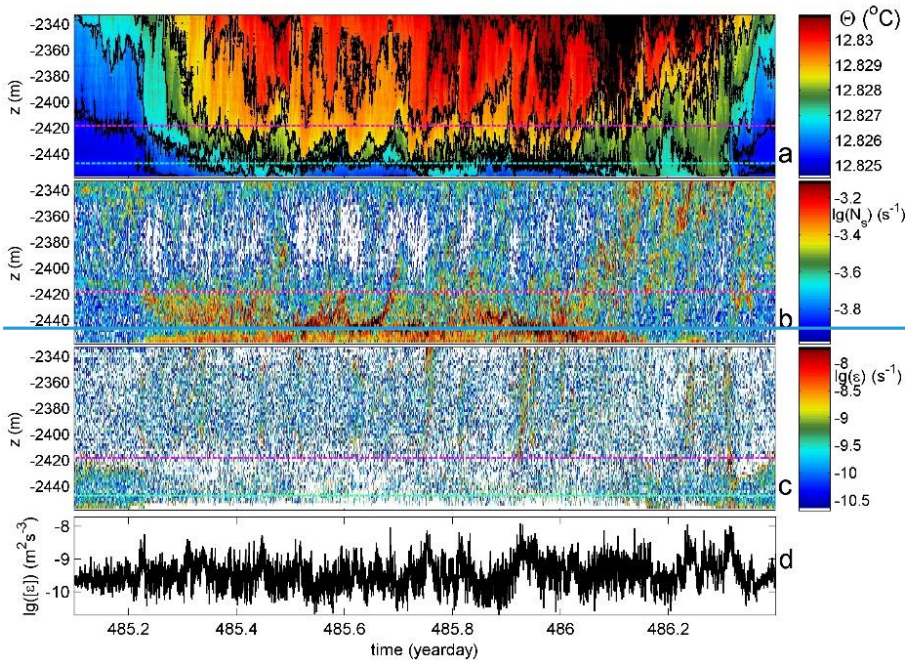
495 **Figure 5.** Overall 20-month time series of moored temperature and current meter data. (a) Conservative
 496 Temperature at h = 1 (cyan), 63 (blue) and 125 m (red) cf. Fig. 4b of arbitrary line 53. Data are not
 497 corrected for electronic-drift bias. The magenta dot indicates day 485. (b) Unfiltered current speed at h
 498 = 126 m of line 14.
 499



500
 501 **Figure 6.** Vertical displacement calculation for vertical lines of the large-ring mooring using the local
 502 adiabatic lapse rate Γ . This height-determination method is based on temperature shift per line after
 503 calibration and drift correction for near-homogeneous period 350.04-350.08, with arbitrary line 53 as
 504 reference. The conversion of meters into degrees Celsius is via $\Gamma = 0.00017^\circ\text{C m}^{-1}$, so that a vertical
 505 difference of $dz = 3$ m reflects approximately 0.0005°C . Corner-lines are 17, 18, 26, 38, 47, 48, 62 and
 506 66.



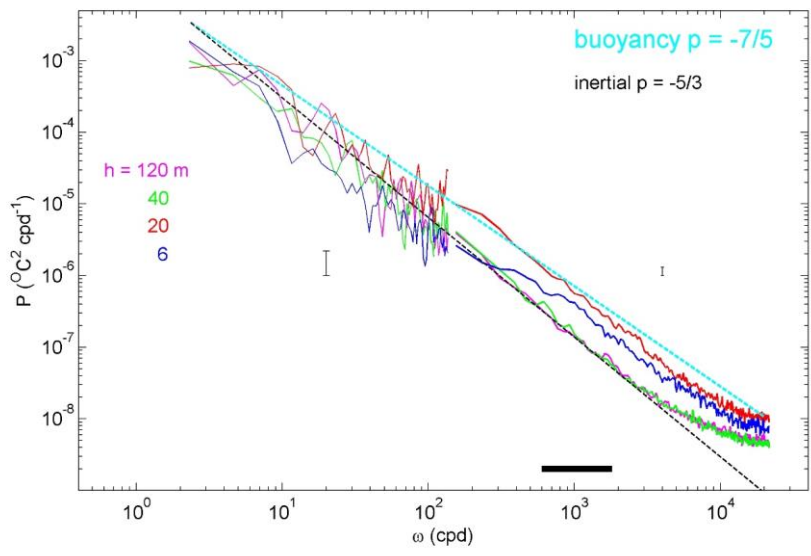
507



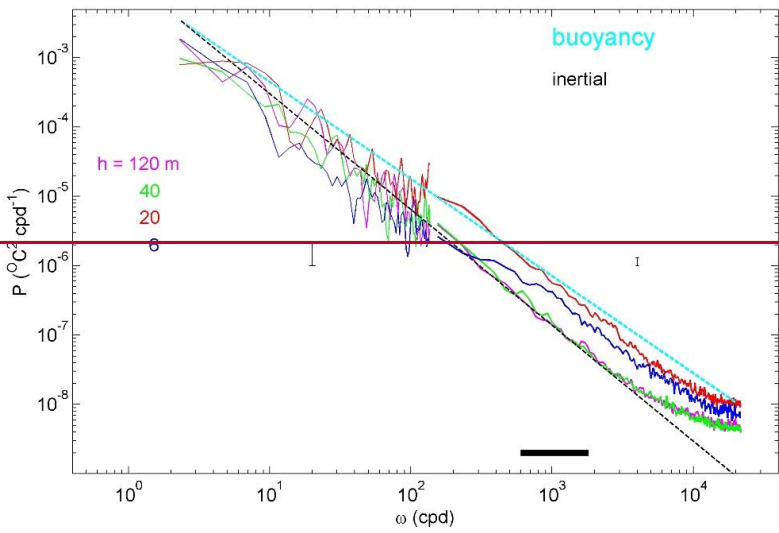
508

509 **Figure 7.** Thirty-one hours of data from line 53 during a turbulent passage of relatively warm water.
510 Horizontal dashed magenta and cyan reference lines are at $h = 40$ and 11 m above seafloor, respectively.
511 (a) Time-depth plot of Conservative Temperature with black-dotted contours every 0.001°C . (b)
512 Logarithm of 2-m small-scale buoyancy frequency from reordered profiles of data in a. (c) Logarithm
513 of non-averaged [displacement values from data in a. following the reordering method by Thorpe \(1977\)](#)
514 [and cast in units of turbulence dissipation rate from data in a.](#) (d) Time series of logarithm of turbulence
515 dissipation rate averaged over the 124-m vertical extent of T-sensors.

516



517



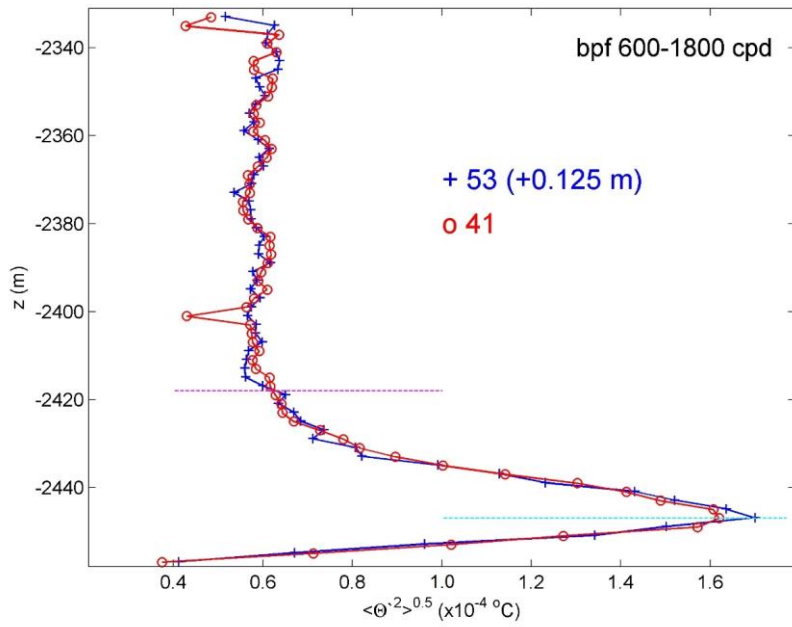
518

519 **Figure 8.** Unscaled frequency spectra, patched from weakly and heavily smoothed parts, for four T-
520 sensors of line 53 at indicated heights h above seafloor, averaged over the 1.3-day period of Fig. 7.

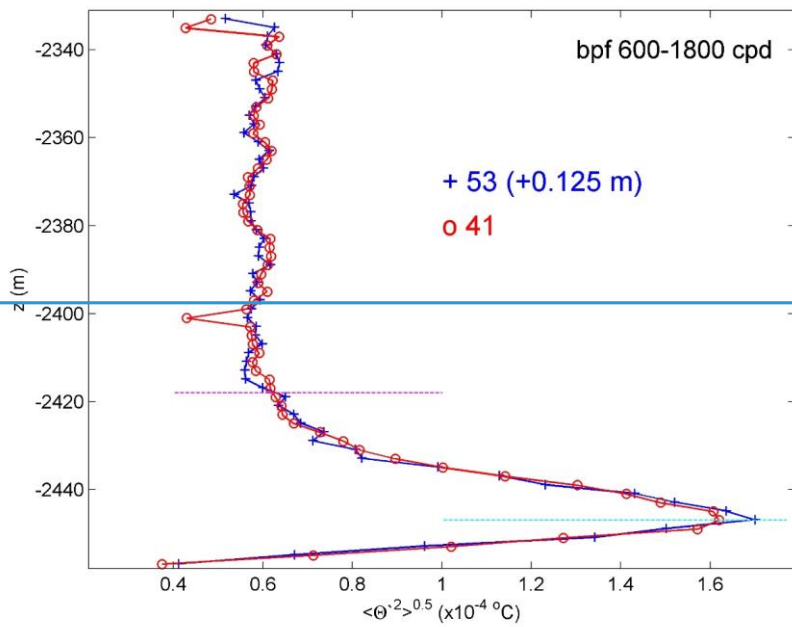
521 Spectral slopes ω_p for inertial and buoyancy subranges (of turbulence) are indicated with straight
522 dashed lines and exponents p. The horizontal black bar indicates frequency range of the pass-filter band
523 that is applied for the turbulence-variance method of height determination.

524

Formatted: Superscript



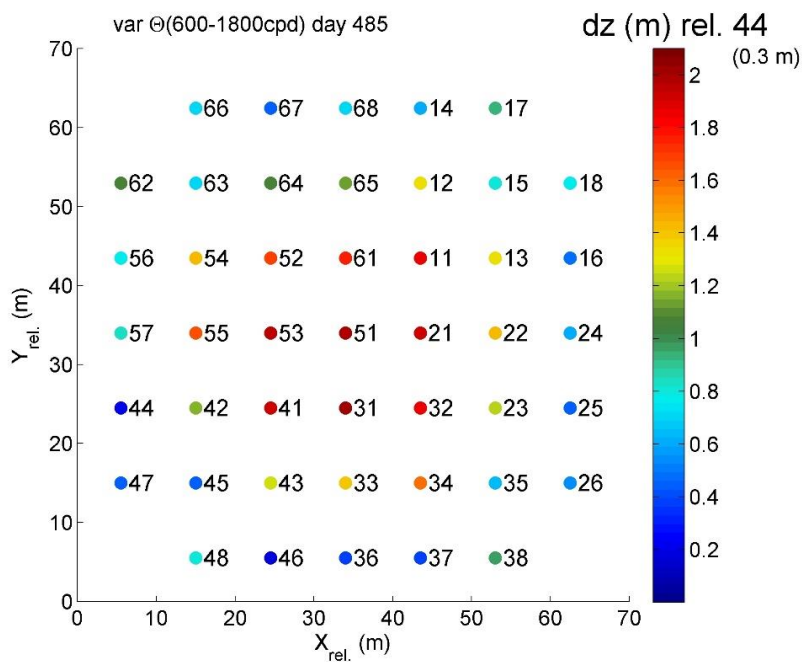
525



526

527 **Figure 9.** Vertical profiles of standard deviation of band-pass filtered ‘bpf’ high-frequency turbulence
 528 signals for temperature data in Figs 7a, 8 for two neighbouring lines, with off-set relative height
 529 determination. The variance-peak height (cyan-dashed line) corresponds also to the height of strongest
 530 layering in stratification (see Fig. 7b). The magenta-dashed line delineates the vertical extent of
 531 enhanced temperature variance above interior values.

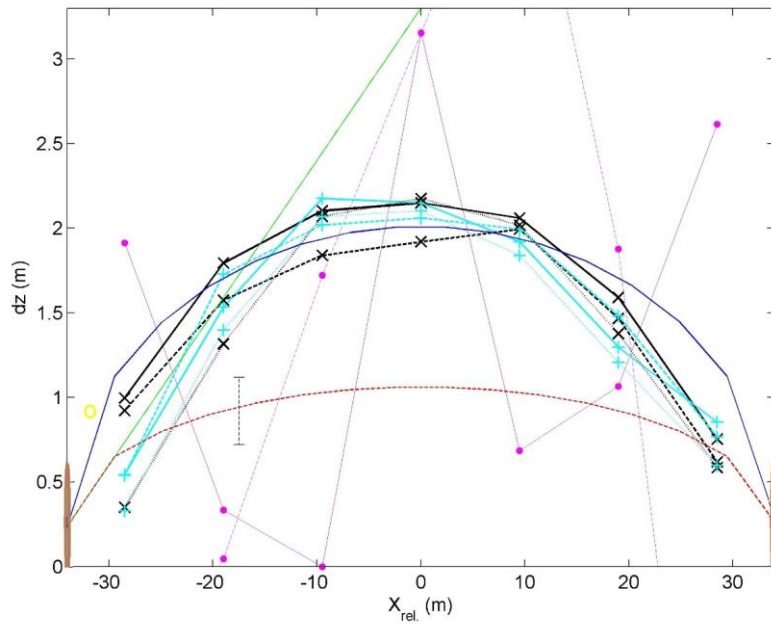
532



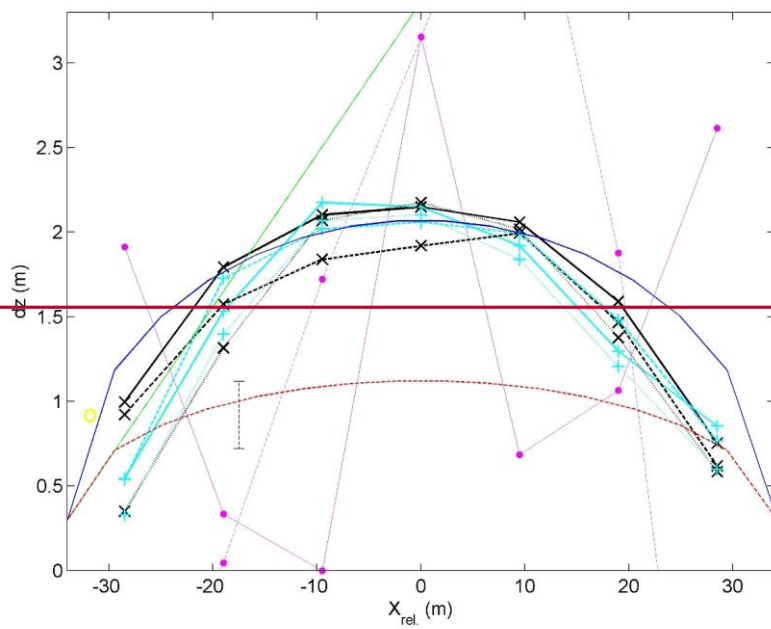
533

534 **Figure 10.** As Fig. 6, but for turbulence-variance height-determination method determined from profiles
 535 like in Fig. 9 using T-sensor data between positions 2 and 3 above seafloor, where the gradient in
 536 temperature variance is maximum, divided by the average gradient over 2 m. Values are given relative
 537 to those of line 44 (0.3 m). [arbitrary line near the edge of the cable-grid.](#)

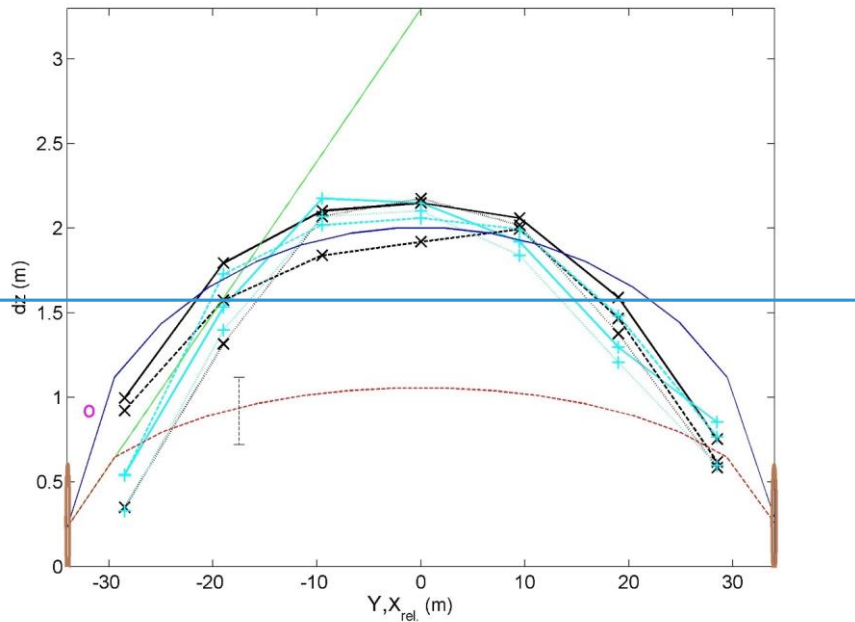
538



539

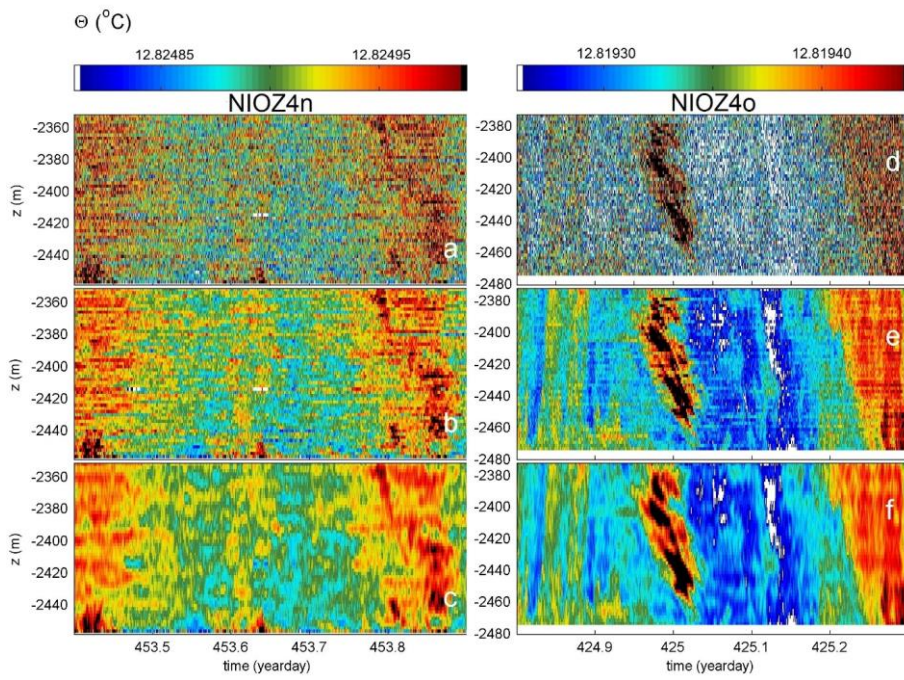


540

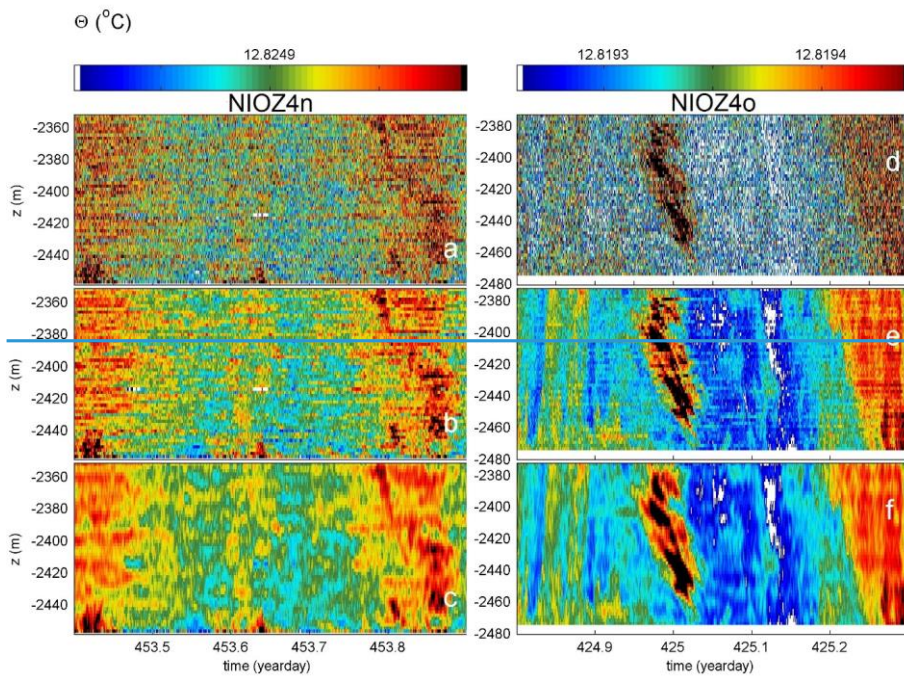


541
 542 **Figure 11.** Constant-Y (black x graphs) and constant-X (cyan +) cross-sections without corner-lines of
 543 height determinations from Fig. 10. Solid lines indicate center lines in both directions. Corner-line height
 544 determination is indicated by yellowmagenta o. For comparison, data in Fig. 6 are given for central lines
 545 with magenta dots (thin solid x-direction; dashed y-direction). In the background, models are given in
 546 green, blue and red of double distance than in Fig. 3.

547

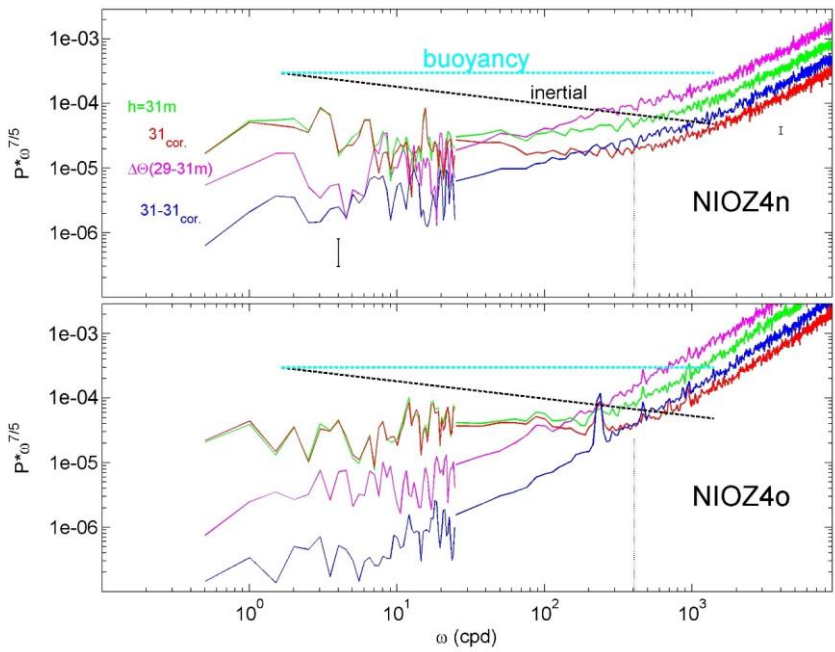


548

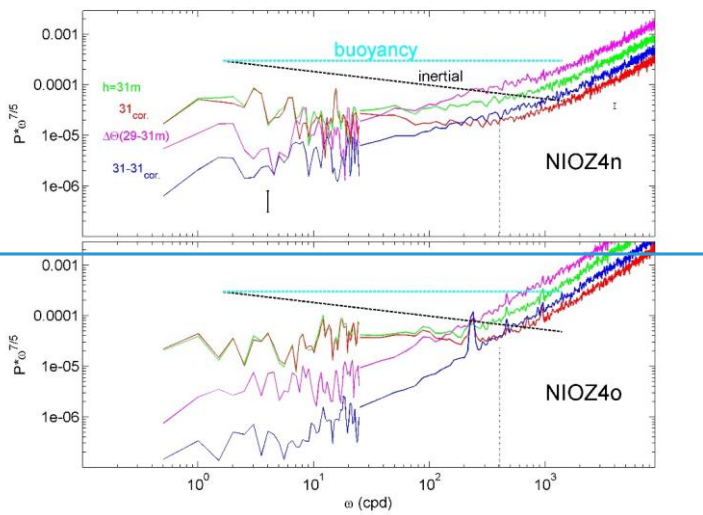


549

550 **Figure A1.** Half-day Conservative-Temperature data from h = 1-104 m demonstrating the correction of
551 short-term drift. The conditions are near homogeneous, as full the temperature range is only 1.7×10^{-4}
552 0.00017°C during **both** the present experiment in 2020/2021 (left column) and during a test-experiment
553 in 22-m deeper water in 2017/2018 (right column). (a, d). Unfiltered data, after post-processing
554 involving calibration, referencing to CTD-, homogeneous-period-, and smooth-polynomial data. (b, e)
555 Low-pass filtered 'lpf' with cut-off at 500 cpd. (c, f) Corrected for short-term drift: 500-cpd and 10-m
556 vertical-scale lpf data.
557



558

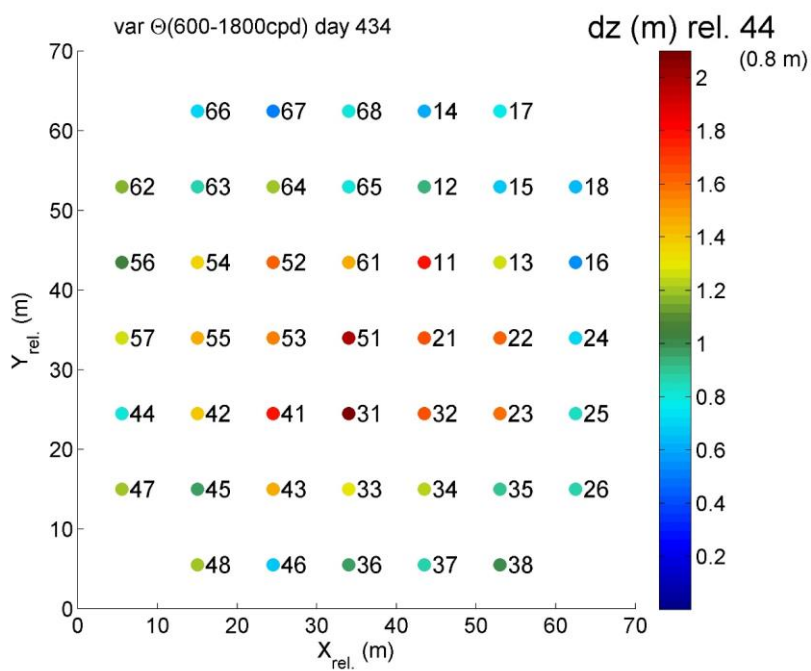


559

560 **Figure A2.** Four-day average spectra that are patched together from two, a weakly- and a heavily
 561 smoothed part, and scaled with the buoyancy-subrange slope (horizontal cyan). The spectra demonstrate
 562 effects of and correction for short-term drift in T-sensor data around $h = 30$ m during near-homogeneous

563 periods between days 453-457, including those of Fig. A1. Plotted are spectra for unfiltered data (green),
 564 vertical temperature difference with data from T-sensor 2-m lower (magenta), 500-cpd and 10-m vertical
 565 scale corrected data (red), and the difference between green and red spectra (blue). For reference, the
 566 relative log-log plot slope is given for inertial subrange (black). The vertical dotted line at 400 cpd is
 567 explained in the text. a) NIOZ4n data. b) NIOZ4o data.

568



569

570 **Figure A3.** As Fig. 10, but for a 3.6 h short warm-water period between days 434.95 and 435.1. The
 571 temperature variance gradient is determined between positions 2 and 4 above seafloor for some
 572 smoothing.

573